

# Measurement of Very-high-energy Diffuse Gamma-ray Emissions from the Galactic Plane with LHAASO-WCDA

Zhen Cao,<sup>1,2,3</sup> F. Aharonian,<sup>4,5</sup> Axikegu,<sup>6</sup> Y.X. Bai,<sup>1,3</sup> Y.W. Bao,<sup>7</sup> D. Bastieri,<sup>8</sup> X.J. Bi,<sup>1,2,3</sup> Y.J. Bi,<sup>1,3</sup> W. Bian,<sup>9</sup> A.V. Bukevich,<sup>10</sup> Q. Cao,<sup>11</sup> W.Y. Cao,<sup>12</sup> Zhe Cao,<sup>13,12</sup> J. Chang,<sup>14</sup> J.F. Chang,<sup>1,3,13</sup> A.M. Chen,<sup>9</sup> E.S. Chen,<sup>1,2,3</sup> H.X. Chen,<sup>15</sup> Liang Chen,<sup>16</sup> Lin Chen,<sup>6</sup> Long Chen,<sup>6</sup> M.J. Chen,<sup>1,3</sup> M.L. Chen,<sup>1,3,13</sup> Q.H. Chen,<sup>6</sup> S. Chen,<sup>17</sup> S.H. Chen,<sup>1,2,3</sup> S.Z. Chen,<sup>1,3</sup> T.L. Chen,<sup>18</sup> Y. Chen,<sup>7</sup> N. Cheng,<sup>1,3</sup> Y.D. Cheng,<sup>1,2,3</sup> M.C. Chu,<sup>19</sup> M.Y. Cui,<sup>14</sup> S.W. Cui,<sup>11</sup> X.H. Cui,<sup>20</sup> Y.D. Cui,<sup>21</sup> B.Z. Dai,<sup>17</sup> H.L. Dai,<sup>1,3,13</sup> Z.G. Dai,<sup>12</sup> Danzengluobu,<sup>18</sup> X.Q. Dong,<sup>1,2,3</sup> K.K. Duan,<sup>14</sup> J.H. Fan,<sup>8</sup> Y.Z. Fan,<sup>14</sup> J. Fang,<sup>17</sup> J.H. Fang,<sup>15</sup> K. Fang,<sup>1,3</sup> C.F. Feng,<sup>22</sup> H. Feng,<sup>1</sup> L. Feng,<sup>14</sup> S.H. Feng,<sup>1,3</sup> X.T. Feng,<sup>22</sup> Y. Feng,<sup>15</sup> Y.L. Feng,<sup>18</sup> S. Gabicci,<sup>23</sup> B. Gao,<sup>1,3</sup> C.D. Gao,<sup>22</sup> Q. Gao,<sup>18</sup> W. Gao,<sup>1,3</sup> W.K. Gao,<sup>1,2,3</sup> M.M. Ge,<sup>17</sup> T.T. Ge,<sup>21</sup> L.S. Geng,<sup>1,3</sup> G. Giacinti,<sup>9</sup> G.H. Gong,<sup>24</sup> Q.B. Gou,<sup>1,3</sup> M.H. Gu,<sup>1,3,13</sup> F.L. Guo,<sup>16</sup> J. Guo,<sup>24</sup> X.L. Guo,<sup>6</sup> Y.Q. Guo,<sup>1,3</sup> Y.Y. Guo,<sup>14</sup> Y.A. Han,<sup>25</sup> O.A. Hannuksela,<sup>19</sup> M. Hasan,<sup>1,2,3</sup> H.H. He,<sup>1,2,3</sup> H.N. He,<sup>14</sup> J.Y. He,<sup>14</sup> Y. He,<sup>6</sup> Y.K. Hor,<sup>21</sup> B.W. Hou,<sup>1,2,3</sup> C. Hou,<sup>1,3</sup> X. Hou,<sup>26</sup> H.B. Hu,<sup>1,2,3</sup> Q. Hu,<sup>12,14</sup> S.C. Hu,<sup>1,3,27</sup> C. Huang,<sup>7</sup> D.H. Huang,<sup>6</sup> T.Q. Huang,<sup>1,3</sup> W.J. Huang,<sup>21</sup> X.T. Huang,<sup>22</sup> X.Y. Huang,<sup>14</sup> Y. Huang,<sup>1,2,3</sup> Y.Y. Huang,<sup>7</sup> X.L. Ji,<sup>1,3,13</sup> H.Y. Jia,<sup>6</sup> K. Jia,<sup>22</sup> H.B. Jiang,<sup>1,3</sup> K. Jiang,<sup>13,12</sup> X.W. Jiang,<sup>1,3</sup> Z.J. Jiang,<sup>17</sup> M. Jin,<sup>6</sup> M.M. Kang,<sup>28</sup> I. Karpikov,<sup>10</sup> D. Khangulyan,<sup>1,3</sup> D. Kuleshov,<sup>10</sup> K. Kurinov,<sup>10</sup> B.B. Li,<sup>11</sup> C.M. Li,<sup>7</sup> Cheng Li,<sup>13,12</sup> Cong Li,<sup>1,3</sup> D. Li,<sup>1,2,3</sup> F. Li,<sup>1,3,13</sup> H.B. Li,<sup>1,3</sup> H.C. Li,<sup>1,3</sup> Jian Li,<sup>12</sup> Jie Li,<sup>1,3,13</sup> K. Li,<sup>1,3</sup> S.D. Li,<sup>16,2</sup> W.L. Li,<sup>22</sup> W.L. Li,<sup>9</sup> X.R. Li,<sup>1,3</sup> Xin Li,<sup>13,12</sup> Y.Z. Li,<sup>1,2,3</sup> Zhe Li,<sup>1,3</sup> Zhuo Li,<sup>29</sup> E.W. Liang,<sup>30</sup> Y.F. Liang,<sup>30</sup> S.J. Lin,<sup>21</sup> B. Liu,<sup>12</sup> C. Liu,<sup>1,3</sup> D. Liu,<sup>22</sup> D.B. Liu,<sup>9</sup> H. Liu,<sup>6</sup> H.D. Liu,<sup>25</sup> J. Liu,<sup>1,3</sup> J.L. Liu,<sup>1,3</sup> M.Y. Liu,<sup>18</sup> R.Y. Liu,<sup>7</sup> S.M. Liu,<sup>6</sup> W. Liu,<sup>1,3</sup> Y. Liu,<sup>8</sup> Y.N. Liu,<sup>24</sup> Q. Luo,<sup>21</sup> Y. Luo,<sup>9</sup> H.K. Lv,<sup>1,3</sup> B.Q. Ma,<sup>29</sup> L.L. Ma,<sup>1,3</sup> X.H. Ma,<sup>1,3</sup> J.R. Mao,<sup>26</sup> Z. Min,<sup>1,3</sup> W. Mitthumsiri,<sup>31</sup> H.J. Mu,<sup>25</sup> Y.C. Nan,<sup>1,3</sup> A. Neronov,<sup>23</sup> K.C.Y. Ng,<sup>19</sup> L.J. Ou,<sup>8</sup> P. Pattarakijwanich,<sup>31</sup> Z.Y. Pei,<sup>8</sup> J.C. Qi,<sup>1,2,3</sup> M.Y. Qi,<sup>1,3</sup> B.Q. Qiao,<sup>1,3</sup> J.J. Qin,<sup>12</sup> A. Raza,<sup>1,2,3</sup> D. Ruffolo,<sup>31</sup> A. Sáiz,<sup>31</sup> M. Saeed,<sup>1,2,3</sup> D. Semikoz,<sup>23</sup> L. Shao,<sup>11</sup> O. Shchegolev,<sup>10,32</sup> X.D. Sheng,<sup>1,3</sup> F.W. Shu,<sup>33</sup> H.C. Song,<sup>29</sup> Yu.V. Stenkin,<sup>10,32</sup> V. Stepanov,<sup>10</sup> Y. Su,<sup>14</sup> D.X. Sun,<sup>12,14</sup> Q.N. Sun,<sup>6</sup> X.N. Sun,<sup>30</sup> Z.B. Sun,<sup>34</sup> J. Takata,<sup>35</sup> P.H.T. Tam,<sup>21</sup> Q.W. Tang,<sup>33</sup> R. Tang,<sup>9</sup> Z.B. Tang,<sup>13,12</sup> W.W. Tian,<sup>2,20</sup> L.H. Wan,<sup>21</sup> C. Wang,<sup>34</sup> C.B. Wang,<sup>6</sup> G.W. Wang,<sup>12</sup> H.G. Wang,<sup>8</sup> H.H. Wang,<sup>21</sup> J.C. Wang,<sup>26</sup> Kai Wang,<sup>7</sup> Kai Wang,<sup>35</sup> L.P. Wang,<sup>1,2,3</sup> L.Y. Wang,<sup>1,3</sup> P.H. Wang,<sup>6</sup> R. Wang,<sup>22</sup> W. Wang,<sup>21</sup> X.G. Wang,<sup>30</sup> X.Y. Wang,<sup>7</sup> Y. Wang,<sup>6</sup> Y.D. Wang,<sup>1,3</sup> Y.J. Wang,<sup>1,3</sup> Z.H. Wang,<sup>28</sup> Z.X. Wang,<sup>17</sup> Zhen Wang,<sup>9</sup> Zheng Wang,<sup>1,3,13</sup> D.M. Wei,<sup>14</sup> J.J. Wei,<sup>14</sup> Y.J. Wei,<sup>1,2,3</sup> T. Wen,<sup>17</sup> C.Y. Wu,<sup>1,3</sup> H.R. Wu,<sup>1,3</sup> Q.W. Wu,<sup>35</sup> S. Wu,<sup>1,3</sup> X.F. Wu,<sup>14</sup> Y.S. Wu,<sup>12</sup> S.Q. Xi,<sup>1,3</sup> J. Xia,<sup>12,14</sup> G.M. Xiang,<sup>16,2</sup> D.X. Xiao,<sup>11</sup> G. Xiao,<sup>1,3</sup> Y.L. Xin,<sup>6</sup> Y. Xing,<sup>16</sup> D.R. Xiong,<sup>26</sup> Z. Xiong,<sup>1,2,3</sup> D.L. Xu,<sup>9</sup> R.F. Xu,<sup>1,2,3</sup> R.X. Xu,<sup>29</sup> W.L. Xu,<sup>28</sup> L. Xue,<sup>22</sup> D.H. Yan,<sup>17</sup> J.Z. Yan,<sup>14</sup> T. Yan,<sup>1,3</sup> C.W. Yang,<sup>28</sup> C.Y. Yang,<sup>26</sup> F. Yang,<sup>11</sup> F.F. Yang,<sup>1,3,13</sup> L.L. Yang,<sup>21</sup> M.J. Yang,<sup>1,3</sup> R.Z. Yang,<sup>12</sup> W.X. Yang,<sup>8</sup> Y.H. Yao,<sup>1,3</sup> Z.G. Yao,<sup>1,3</sup> L.Q. Yin,<sup>1,3</sup> N. Yin,<sup>22</sup> X.H. You,<sup>1,3</sup> Z.Y. You,<sup>1,3</sup> Y.H. Yu,<sup>12</sup> Q. Yuan,<sup>14</sup> H. Yue,<sup>1,2,3</sup> H.D. Zeng,<sup>14</sup> T.X. Zeng,<sup>1,3,13</sup> W. Zeng,<sup>17</sup> M. Zha,<sup>1,3</sup> B.B. Zhang,<sup>7</sup> F. Zhang,<sup>6</sup> H. Zhang,<sup>9</sup> H.M. Zhang,<sup>7</sup> H.Y. Zhang,<sup>17</sup> J.L. Zhang,<sup>20</sup> Li Zhang,<sup>17</sup> P.F. Zhang,<sup>17</sup> P.P. Zhang,<sup>12,14</sup> R. Zhang,<sup>14</sup> S.B. Zhang,<sup>2,20</sup> S.R. Zhang,<sup>11</sup> S.S. Zhang,<sup>1,3</sup> X. Zhang,<sup>7</sup> X.P. Zhang,<sup>1,3</sup> Y.F. Zhang,<sup>6</sup> Yi Zhang,<sup>1,14</sup> Yong Zhang,<sup>1,3</sup> B. Zhao,<sup>6</sup> J. Zhao,<sup>1,3</sup> L. Zhao,<sup>13,12</sup> L.Z. Zhao,<sup>11</sup> S.P. Zhao,<sup>14</sup> X.H. Zhao,<sup>26</sup> F. Zheng,<sup>34</sup> W.J. Zhong,<sup>7</sup> B. Zhou,<sup>1,3</sup> H. Zhou,<sup>9</sup> J.N. Zhou,<sup>16</sup> M. Zhou,<sup>33</sup> P. Zhou,<sup>7</sup> R. Zhou,<sup>28</sup> X.X. Zhou,<sup>1,2,3</sup> X.X. Zhou,<sup>6</sup> B.Y. Zhu,<sup>12,14</sup> C.G. Zhu,<sup>22</sup> F.R. Zhu,<sup>6</sup> H. Zhu,<sup>20</sup> K.J. Zhu,<sup>1,2,3,13</sup> Y.C. Zou,<sup>35</sup> and X. Zuo<sup>1,3</sup>

(The LHAASO Collaboration)\*

<sup>1</sup>Key Laboratory of Particle Astrophysics & Experimental Physics Division & Computing Center, Institute of High Energy Physics, Chinese Academy of Sciences, 100049 Beijing, China

<sup>2</sup>University of Chinese Academy of Sciences, 100049 Beijing, China

<sup>3</sup>TIANFU Cosmic Ray Research Center, Chengdu, Sichuan, China

<sup>4</sup>Dublin Institute for Advanced Studies, 31 Fitzwilliam Place, 2 Dublin, Ireland

<sup>5</sup>Max-Planck-Institut für Kernphysik, P.O. Box 103980, 69029 Heidelberg, Germany

<sup>6</sup>School of Physical Science and Technology & School of Information Science and Technology, Southwest Jiaotong University, 610031 Chengdu, Sichuan, China

<sup>7</sup>School of Astronomy and Space Science, Nanjing University, 210023 Nanjing, Jiangsu, China

<sup>8</sup>Center for Astrophysics, Guangzhou University, 510006 Guangzhou, Guangdong, China

<sup>9</sup>Tsung-Dao Lee Institute & School of Physics and Astronomy, Shanghai Jiao Tong University, 200240 Shanghai, China

<sup>10</sup>Institute for Nuclear Research of Russian Academy of Sciences, 117312 Moscow, Russia

<sup>11</sup>Hebei Normal University, 050024 Shijiazhuang, Hebei, China

<sup>12</sup>University of Science and Technology of China, 230026 Hefei, Anhui, China

<sup>13</sup>State Key Laboratory of Particle Detection and Electronics, China

<sup>14</sup>Key Laboratory of Dark Matter and Space Astronomy & Key Laboratory of Radio Astronomy, Purple Mountain Observatory, Chinese Academy of Sciences, 210023 Nanjing, Jiangsu, China

<sup>15</sup>Research Center for Astronomical Computing, Zhejiang Laboratory, 311121 Hangzhou, Zhejiang, China

<sup>16</sup>Key Laboratory for Research in Galaxies and Cosmology,

Shanghai Astronomical Observatory, Chinese Academy of Sciences, 200030 Shanghai, China

<sup>17</sup>School of Physics and Astronomy, Yunnan University, 650091 Kunming, Yunnan, China

- <sup>18</sup>Key Laboratory of Cosmic Rays (Tibet University), Ministry of Education, 850000 Lhasa, Tibet, China
- <sup>19</sup>Department of Physics, The Chinese University of Hong Kong, Shatin, New Territories, Hong Kong, China
- <sup>20</sup>Key Laboratory of Radio Astronomy and Technology,  
National Astronomical Observatories, Chinese Academy of Sciences, 100101 Beijing, China
- <sup>21</sup>School of Physics and Astronomy (Zhuhai) & School of Physics (Guangzhou)  
& Sino-French Institute of Nuclear Engineering and Technology (Zhuhai),  
Sun Yat-sen University, 519000 Zhuhai & 510275 Guangzhou, Guangdong, China
- <sup>22</sup>Institute of Frontier and Interdisciplinary Science, Shandong University, 266237 Qingdao, Shandong, China
- <sup>23</sup>APC, Université Paris Cité, CNRS/IN2P3, CEA/IRFU, Observatoire de Paris, 119 75205 Paris, France
- <sup>24</sup>Department of Engineering Physics & Department of Astronomy, Tsinghua University, 100084 Beijing, China
- <sup>25</sup>School of Physics and Microelectronics, Zhengzhou University, 450001 Zhengzhou, Henan, China
- <sup>26</sup>Yunnan Observatories, Chinese Academy of Sciences, 650216 Kunming, Yunnan, China
- <sup>27</sup>China Center of Advanced Science and Technology, Beijing 100190, China
- <sup>28</sup>College of Physics, Sichuan University, 610065 Chengdu, Sichuan, China
- <sup>29</sup>School of Physics, Peking University, 100871 Beijing, China
- <sup>30</sup>Guangxi Key Laboratory for Relativistic Astrophysics,  
School of Physical Science and Technology, Guangxi University, 530004 Nanning, Guangxi, China
- <sup>31</sup>Department of Physics, Faculty of Science, Mahidol University, Bangkok 10400, Thailand
- <sup>32</sup>Moscow Institute of Physics and Technology, 141700 Moscow, Russia
- <sup>33</sup>Center for Relativistic Astrophysics and High Energy Physics,  
School of Physics and Materials Science & Institute of Space Science and Technology,  
Nanchang University, 330031 Nanchang, Jiangxi, China
- <sup>34</sup>National Space Science Center, Chinese Academy of Sciences, 100190 Beijing, China
- <sup>35</sup>School of Physics, Huazhong University of Science and Technology, Wuhan 430074, Hubei, China

(Dated: November 28, 2024)

The diffuse Galactic gamma-ray emission is a very important tool used to study the propagation and interaction of cosmic rays in the Milky Way. In this work, we report the measurements of the diffuse emission from the Galactic plane, covering Galactic longitudes from  $15^\circ$  to  $235^\circ$  and latitudes from  $-5^\circ$  to  $+5^\circ$ , in an energy range of 1 TeV to 25 TeV, with the Water Cherenkov Detector Array (WCDA) of the Large High Altitude Air Shower Observatory (LHAASO). After masking the sky regions of known sources, the diffuse emission is detected with  $24.6\sigma$  and  $9.1\sigma$  significance in the inner Galactic plane ( $15^\circ < l < 125^\circ$ ,  $|b| < 5^\circ$ ) and outer Galactic plane ( $125^\circ < l < 235^\circ$ ,  $|b| < 5^\circ$ ), respectively. The WCDA spectra in both regions can be well described by a power-law function, with spectral indices of  $-2.67 \pm 0.05_{\text{stat}}$  in the inner region and  $-2.83 \pm 0.19_{\text{stat}}$  in the outer region, respectively. Combined with the Square Kilometer Array (KM2A) measurements at higher energies, a clear softening of the spectrum is found in the inner region, with change of spectral indices by  $\sim 0.5$  at a break energy around 30 TeV. The fluxes of the diffuse emission are higher by a factor of 1.5 – 2.7 than the model prediction assuming local CR spectra and the gas column density, which are consistent with those measured by the KM2A. Along Galactic longitude, the spatial distribution of the diffuse emission shows deviation from that of the gas column density. The spectral shape of the diffuse emission are possibly variation in different longitude region. The WCDA measurements bridge the gap between the low-energy measurements by space detectors and the ultra-high-energy observations by LHAASO-KM2A and other experiments. The results indicate further that the conventional model prediction of diffuse emission from cosmic ray interactions is not enough to account for the observations.

PACS numbers: 95.85.Pw, 98.70.Sa

*Introduction.* — One of the most important unresolved problems in astrophysics is the origin and propagation of cosmic rays (CRs). Besides the direct measurements of energy spectra and arrival directions of individual composition of CRs, the diffuse  $\gamma$ -ray emission plays a unique and complementary role in constraining the origin and propagation of CRs. The diffuse  $\gamma$ -ray emission is usually expected to be produced through interactions between CRs (nuclei and electrons/positrons) and the interstellar medium (ISM) or radiation field [1–3]. Modeling of the diffuse emission in the high-energy  $\gamma$ -ray bands (HE,  $\lesssim 0.1$  TeV) is in general consistent

with the all-sky measurements by Fermi Large Area Telescope [4], supporting the basic framework of CR propagation and interaction in the Milky Way.

Measurements of the wide-band diffuse  $\gamma$ -ray emission is particularly important in constraining the origin and testing the propagation models of CRs. Due either to the small field-of-view of imaging atmospheric Cherenkov telescope arrays or the limited sensitivity of extensive air shower detector arrays, the observations of diffuse  $\gamma$ -ray emission have been challenging for groundbased experiments for a long time. A few measurements have been reported by MILAGRO [5, 6], H.E.S.S. [7], ARGO-YBJ [8], AS $\gamma$  [9], and HAWC [10]. Particularly, the recent precise measurement by the Square Kilometer Array (KM2A) of the Large High Altitude Air Shower Observatory (LHAASO) [11] in the energy range from 10 to

\* E-mail: lihuicai@ihep.ac.cn; ppzhang@pmo.ac.cn; hushicong@ihep.ac.cn; yuanq@pmo.ac.cn; yaozg@ihep.ac.cn; guoyq@ihep.ac.cn

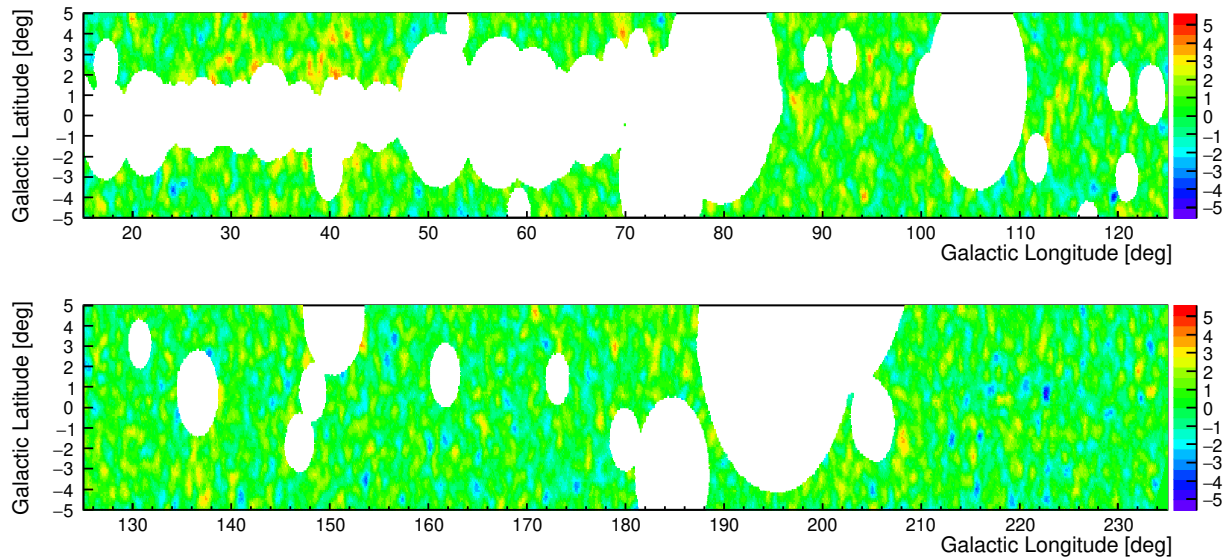


FIG. 1. The significance maps in Galactic coordinate of the inner Galaxy region (top panel) and outer Galaxy region (bottom panel) for  $N_{\text{hit}} \geq 200$  (corresponding to energies bigger than several TeV) after masking the resolved LHAASO and TeVCat sources.

1000 TeV, together with the Fermi measurement in space below TeV energy [12], gives the diffuse emission in a very wide energy range and offers new insights in understanding the origin of the diffuse  $\gamma$ -rays and the propagation model of CRs (e.g., [13–16]). Nevertheless, the detection of diffuse emission in energy range from 1 to 10 TeV is still lacking, which hinders a good discrimination of different models. In this work, we report the measurement of diffuse  $\gamma$ -ray emission from the Galactic plane in the energy range from 1 to 25 TeV using the Water Cherenkov Detector Array (WCDA) of the LHAASO experiment. The energy coverage of WCDA fills the gap between Fermi and LHAASO-KM2A. Together with Fermi and KM2A, the Galactic diffuse emission covering an energy range of more than 6 orders of magnitude (from sub-GeV to PeV) will be obtained for the first time.

*The LHAASO experiment.* — The LHAASO [17] is a multi-component CR and  $\gamma$ -ray detection facility located on Haizi Mountain about 4410 meters above sea level in Daocheng, Sichuan province, China. It is designed to detect air showers induced by CR particles with energies from  $\sim$ TeV to  $\sim$ EeV and by photons from  $\sim$  100 GeV to  $>$ PeV. The WCDA is one of the three major components of LHAASO. It is a close-packed, surface water Cherenkov detector facility with an area of 78,000 m<sup>2</sup>. The WCDA consists of three ponds, two of them have an area of  $150 \times 150$  m<sup>2</sup> with 900 detector units each, and the third one has an area of  $300 \times 110$  m<sup>2</sup> with 1320 detector units. The primary goal of WCDA is to survey the northern  $\gamma$ -ray sky in the very-high-energy (VHE) band [17, 18]. The large field-of-view and high sensitivity of WCDA makes it a powerful detector for the study of diffuse  $\gamma$ -ray emission.

*Data analysis.* — The data used in this work is collected by WCDA between March 5, 2021 and July 31, 2023. After quality cuts, the total live time is 763 days. The event

selection criteria are the same as in Ref. [19]. The parameter PINcness, defined as  $\mathcal{P} = \frac{1}{N} \sum_{i=1}^N \frac{(\zeta_i - \langle \zeta_i \rangle)^2}{\sigma_{\zeta_i}^2}$ , where  $\zeta_i$  is the logarithm of the  $i$ -th PMT charge,  $\langle \zeta_i \rangle$  and  $\sigma_{\zeta_i}$  are the average value and dispersion of a sample of gamma-like events, is applied to exclude hadronic showers [20]. In this work we set  $\mathcal{P} < 1.1$ . The region of interesting (ROI) is same as that used in the KM2A analysis [11], i.e., the inner Galactic plane ( $15^\circ < l < 125^\circ$ ,  $|b| < 5^\circ$ ) and the outer Galactic plane ( $125^\circ < l < 235^\circ$ ,  $|b| < 5^\circ$ ). The analysis in different longitude regions are also performed. The events are binned by number of hits in six bins, i.e., 60-100, 100-200, 200-300, 300-500, 500-800,  $\geq 800$ , which represent increasing energies from  $\sim$  1 TeV to  $\sim$  25 TeV. For the outer region, the measurement is performed for the last four bins to keep a relatively high significance. We also update the KM2A results for  $25 < E < 1000$  TeV, following the analysis of [11], but using the full array data from July 20, 2021 to July 31, 2023 and the updated source mask compared to the one used in this work.

The background, mainly from residual CR events, is estimated using the “direct integral method” [21]. This method assumes that the detection efficiency is slowly varying and the time-average within a relatively short time window can properly reflect the background content. The time step to calculate the background is chosen to be 1 hour, and the time window is chosen to be  $\pm 5$  hours of each step. Some spurious large-scale structures of the background may exist, which have been corrected in the analysis (see Fig. S1 of the Supplemental Material) [11]. Quite a number of pointlike and extended sources have been detected [19, 22, 23]. To reduce the impact of  $\gamma$ -rays sources on the background estimate, we mask the Galactic plane with latitudes  $|b| \leq 10^\circ$  for declinations  $\delta \leq 50^\circ$  and  $|b| \leq 5^\circ$  for  $\delta > 50^\circ$ . The sky regions around sources out of the Galactic plane, based on the TeVCat as of December 2022 [24] and WCDA/KM2A source list [19],



are also masked. The mask radius is chosen to be 5 times of  $\sigma \equiv \sqrt{\sigma_{\text{ext}}^2 + \sigma_{\text{psf}}^2}$ , where  $\sigma_{\text{ext}}$  is the fitted Gaussian extension of the source and  $\sigma_{\text{psf}}$  is the Gaussian width of the point spread function of WCDA. In this work we adopt  $\sigma_{\text{psf}} = 0.5^\circ$  for all energy bins to keep the same sky regions.

To measure the diffuse emission, we also mask known sources detected by LHAASO [19] and those listed in TeVCat [24], with different mask radii, to balance the remaining sky region and the impacts from sources. We adopt a mask radius of 2.5 times of  $\sigma$  as defined above for each source. For pulsar halos Geminga and Monogem, whose morphologies are not well described by simple Gaussian functions, the mask radius is set to be  $8^\circ$  which can largely remove the emission from these two sources. The regions of interest (ROI) can be seen in Fig. 1, where blank regions are masked out. Since the source list and source extensions of WCDA are different from those of KM2A, the ROIs also differ slightly from the previous KM2A analysis [11]. Specifically, the solid angle of the ROI is 0.172 (0.255) for the inner (outer) region in this work, compared with 0.206 (0.268) of the previous KM2A ROI [11]. We also estimate the residual contamination from resolved sources, through a fitting of the morphological distribution of the data for different rings surrounding resolved sources (represented by the multiplicative factor of source extension  $\sigma$ ), using simulated templates of resolved sources and the diffuse emission. See Fig. S2 of the Supplemental Material for illustration. The contamination fraction, given in Table S1 of the Supplemental Material, will be subtracted when evaluating the diffuse fluxes.

A likelihood fitting method is employed to derive the flux of the diffuse emission, in the whole energy band or individual energy bin. To properly account for the spectral shape of the emission in a wide energy band, from TeV to PeV, a smoothly broken power-law (SBPL) function,  $\phi(E) = \phi_0 (E/10 \text{ TeV})^{-\alpha} [1 + (E/E_{\text{br}})^s]^{(\alpha-\beta)/s}$ , is assumed, where  $E_{\text{br}}$  is the break energy,  $\alpha$  and  $\beta$  are the photon indices before and after the break, and  $s$  characterizes the smoothness of the break which is fixed to be 5 in this work. For the fitting of the WCDA data alone in a limited energy range, we assume a power-law spectrum  $\phi(E) = \phi_0 (E/10 \text{ TeV})^{-\alpha}$  instead. The test statistic (TS) is defined as two times of the logarithmic likelihood ratio of the signal plus background hypothesis ( $H_1$ ) and the background only hypothesis ( $H_0$ ), i.e.,  $\text{TS} = 2 \ln(\mathcal{L}_{s+b}/\mathcal{L}_b)$ . The TS value follows approximately a  $\chi^2$  distribution with two (four) degrees of freedom for PL (SBPL) model. The forward-folding method is used to determine the model parameters, i.e., for a given set of model parameters, we convolve the instrumental response functions to get the expected number of events, and then construct the Poisson likelihood according to the observations.

*Results on diffuse emission.* — Fig. 1 shows the significance maps for  $N_{\text{hit}} \geq 200$  in Galactic coordinate for the inner (top panel) and outer (bottom panel) regions, respectively. The one-dimensional significance distributions of these two regions and the control regions shifted by  $20^\circ$  in Galactic latitudes are given in Fig. S3 of the Supplemental Material. The detection significance of diffuse emission is about  $24.6\sigma$  ( $9.1\sigma$ ) in the inner (outer) region. For the first time, the multi-

TeV diffuse emission in the outer Galactic plane is detected by LHAASO-WCDA.

The spectral energy distributions (SED) of the diffuse emission from  $\sim$ TeV to PeV in the two regions are given in Fig. 2. The shorter error bars represent the statistical errors, and the longer ones are the quadratic sum of the statistical errors and the systematical uncertainties (see below for details). The data of the fluxes together with the statistical and systematic uncertainties can be found in Tables S2 and S3 of the Supplemental Material. The diffuse  $\gamma$ -ray fluxes are lower by a factor of several than those of CR electrons and positrons [25–27], as shown in Fig. S4 of the Supplemental Material. However, in our data-driven background estimate method, the electron and positron background is largely suppressed given their nearly isotropic spatial distribution. For a better comparison with the neutrino emission [28], we also present the total fluxes without source masks in Fig. S5 of the Supplemental Material.

The wide-band spectra are fitted with the SBPL function, with parameters being presented in Table I. The fitting results indicate that breaks of the spectra, around 30 TeV, exist. Quantitatively, a single power-law fitting gives a TS value of 1099.10 (272.29) for the inner (outer) region, while the SBPL fitting gives 1131.25 (273.40). Therefore, the significance of the spectral break in the inner region is about  $5.3\sigma$ , given two more free parameters. For the outer region the break is not statistically significant. Within the statistical uncertainties, the spectral parameters in the inner and outer Galactic plane are consistent with each other. We further divide the inner region into three sub-regions, with Galactic longitudes of  $l \in [15^\circ, 50^\circ]$ ,  $l \in [50^\circ, 90^\circ]$  and  $l \in [90^\circ, 125^\circ]$ , and re-fit their spectra. The results are shown in Fig. 3. The spectral index of the third sub-region is found to be slightly harder ( $\sim 2\sigma$  significance) than the other two sub-regions, as can be seen in Table II. Such differences remain for the background estimate with different mask region ( $|b| < 10^\circ$ ) and time window (24 hours). These results indicate that spectral variations may exist across the Galactic plane.

We also derive the spatial distributions of the WCDA diffuse emission along Galactic latitudes and longitudes, as shown in Fig. 4. The results are compared with the gas distributions obtained from the sum of atomic hydrogen from the HI4PI survey [29], molecular hydrogen from the CO survey [30] with a CO-to- $\text{H}_2$  conversion factor of  $X_{\text{CO}} = 1.6 \times 10^{20} \text{ cm}^2 (\text{K km s}^{-1})^{-1}$  [4], and an ionized hydrogen component from the model of [31]. It is shown that the latitude distributions are roughly consistent with the gas distributions in both the inner and outer regions. The fitting of the gas template to the data gives  $p$ -values of 0.003 – 0.013 of the two regions. However, the longitude distribution deviates clearly from the gas distribution. The gas template fitting shows a  $p$ -value of  $6.0 \times 10^{-21}$ . Similar results have also been obtained for the KM2A measurements at higher energies [11] (see Fig. S6 of the Supplemental Material for the comparison between WCDA and KM2A).

*Systematic uncertainties.* — One of the major sources of systematic uncertainties is the background estimate. We vary the time window from  $\pm 5$  hours to  $\pm 12$  hours, and also change

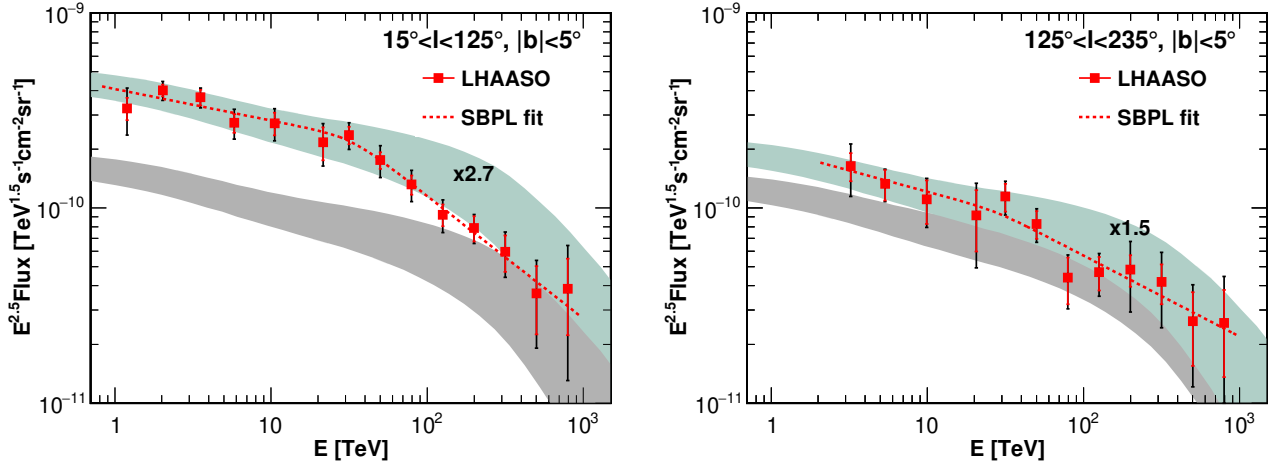


FIG. 2. SEDs of the diffuse  $\gamma$ -ray emission in the inner (left) and outer (right) regions. Error bars are the statistical errors (short red) and the quadratic sum of the statistical and systematic errors (long black). Dashed lines show the best-fit SBPL spectra. The grey shaded bands show the predicted diffuse fluxes from local CR intensities and the line-of-sight integral gas content, and the cyan bands are upscaled by constant factors as labelled in the plots.

TABLE I. SBPL fitting parameters of the wide-band diffuse emission measured by WCDA and KM2A

Region	$\phi_0$ at 10 TeV ( $10^{-13} \text{ TeV}^{-1} \text{ cm}^{-2} \text{ s}^{-1} \text{ sr}^{-1}$ )	$\alpha$	$\beta$	$E_{\text{br}}$ (TeV)
$15^\circ < l < 125^\circ$ (inner)	$8.88 \pm 0.53_{\text{stat}}$	$-2.66 \pm 0.05_{\text{stat}}$	$-3.13 \pm 0.08_{\text{stat}}$	$32.84 \pm 11.16_{\text{stat}}$
$125^\circ < l < 235^\circ$ (outer)	$3.84 \pm 0.37_{\text{stat}}$	$-2.72 \pm 0.10_{\text{stat}}$	$-2.92 \pm 0.10_{\text{stat}}$	$27.86 \pm 22.49_{\text{stat}}$

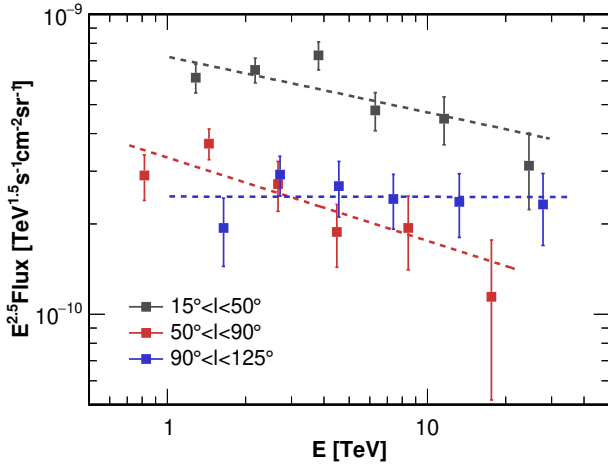


FIG. 3. Fluxes of diffuse  $\gamma$ -ray emission in the three sub-regions of the inner Galactic plane measured by the WCDA. Only the statistical errors are shown.

the mask regions for background estimate to  $|b| \leq 10^\circ$  for all declinations to obtain the variations of the results. The other effect related with the background is the spurious large-scale efficiency correction (see Sec. B of the Supplemental

TABLE II. Power-law fitting results of the LHAASO-WCDA diffuse emission.

Region	$\phi_0$ at 10 TeV ( $10^{-13} \text{ TeV}^{-1} \text{ cm}^{-2} \text{ s}^{-1} \text{ sr}^{-1}$ )	$\alpha$
$15^\circ < l < 125^\circ$ (inner)	$8.50 \pm 0.58_{\text{stat}}$	$-2.67 \pm 0.05_{\text{stat}}$
$125^\circ < l < 235^\circ$ (outer)	$3.49 \pm 0.55_{\text{stat}}$	$-2.83 \pm 0.19_{\text{stat}}$
$15^\circ < l < 50^\circ$	$14.88 \pm 1.26_{\text{stat}}$	$-2.69 \pm 0.06_{\text{stat}}$
$50^\circ < l < 90^\circ$	$5.55 \pm 0.91_{\text{stat}}$	$-2.78 \pm 0.09_{\text{stat}}$
$90^\circ < l < 125^\circ$	$7.79 \pm 0.81_{\text{stat}}$	$-2.50 \pm 0.09_{\text{stat}}$

Material), for which we adopt different smoothing angles of  $15^\circ$ ,  $20^\circ$ ,  $25^\circ$ , and  $30^\circ$ . We find that the impacts of those changes on parameters  $\phi_0$  are about 6% (16%) and on  $\alpha$  are about 0.05 (0.13), for the inner (outer) region. The variation of the atmosphere condition during the operation affects the detection efficiency, which is not properly modelled in the simulation. For point-like sources this effect is estimated to be about 8% for the flux ( $\phi_0$ ) and 0.02 for the spectral index ( $\alpha$ ) [19]. Similar impacts on the diffuse emission is expected. Combining these results, we obtain the total systematic uncertainties as 10% (18%) for  $\phi_0$  and 0.05 (0.13) for  $\alpha$ , for the inner (outer) region, respectively. The discussion of systematic uncertainties of the KM2A results can be referred to Ref. [11]. The systematic uncertainty of the flux in each en-

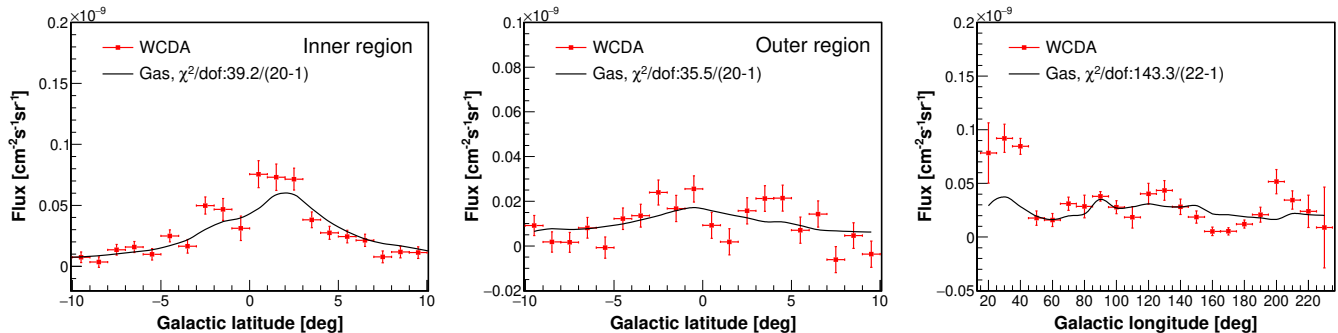


FIG. 4. Galactic latitude and longitude profiles of the diffuse fluxes for  $N_{\text{hit}} \geq 200$  (corresponding to an energy range of about 3 – 25 TeV), compared with the gas distributions as shown by solid lines.

ergy bin has been shown in Fig. 2 and also in Tables S2 and S3 of the Supplemental Material.

*Discussion.* — We compare the data with the predictions of the hadronic interactions between CRs and the ISM. We adopt the parameterizations of the local proton and helium spectra as given in Ref. [11], which include the uncertainties of the current measurements, especially for those measured by indirect detection experiments above  $\sim 100$  TeV. We assume that the CR intensity is uniform in the Galaxy, and calculate the  $\gamma$ -ray emission using the local CR spectra and the line-of-sight integrated gas content. The  $\gamma$ -ray production cross section used is from the AAfrag package [32]. The expected diffuse  $\gamma$ -ray fluxes are shown by grey shaded bands in Fig. 2. We can see that in the inner region the measurements are higher by a factor of  $\sim 2.7$  than the prediction, and in the outer region the measurements are higher by  $\sim 1.5$  times. These results are consistent with those found in the LHAASO-KM2A analysis [11]. The HAWC measurements in a different sky region of the inner Galaxy also showed a factor of 2 higher fluxes compared with a DRAGON model prediction [10]. The spectral shape of the prediction is slightly different from the measurement in the inner region from tens of TeV to PeV. However, in the outer region, the predicted spectrum is consistent with the data within uncertainties. We point out that the observed spectral break around 30 TeV in  $\gamma$  rays may not correspond to the knee of CRs which is expected to break in hundreds of TeV given that the current measured spectra of protons and helium show the knee feature around several PeV [33, 34]. More data are needed to clarify whether there are imprints of the knee feature in the diffuse  $\gamma$ -ray spectra.

The break may be due to the addition of an unresolved source population whose spectrum show a cutoff around tens of TeV. If we compare the data (including those measured by Fermi-LAT between 1 and 500 GeV [12], updated with the new mask of this work) with the model prediction<sup>1</sup> in a wider energy range, from GeV to PeV, we find that the excess mainly

exists from several GeV to tens of TeV (see Fig. 5). Such an excess may come from a population of unresolved, low surface brightness sources such as pulsar wind nebulae or pulsar halos [1, 13, 16, 37, 38]. The spatial variations of the spectra of the diffuse emission may further supports the hypothesis that unresolved sources may exist, although other possibilities such as spatially-dependent spectral slopes of CRs can not be excluded. Following Ref. [12], we add an empirical component with spectrum  $\propto E^{-2.45} \exp(-E/20 \text{ TeV})$  to the CR propagation model prediction, and find a good agreement with the wide-band measurements, as shown in Fig. 5. Other sources like young massive star clusters [39], the confinement and interaction of CRs around acceleration sources [40–42], as well as the change of the canonical propagation scenario [43–46] were also discussed in literature. The multi-messenger analysis of the diffuse  $\gamma$  rays and neutrinos [28] would be helpful in understanding the nature of the diffuse emission.

*Summary.* — In this work we measure the diffuse  $\gamma$ -ray emission in an energy range of about 1 – 25 TeV from the Galactic plane using the LHAASO-WCDA data. The detection significance of the diffuse emission, after masking sky regions around resolved sources, is  $24.6\sigma$  for the inner Galactic plane ( $15^\circ < l < 125^\circ$ ,  $|b| < 5^\circ$ ) and  $9.1\sigma$  for the outer Galactic plane ( $125^\circ < l < 235^\circ$ ,  $|b| < 5^\circ$ ) regions, respectively. The diffuse emission from the outer Galactic plane is for the first time detected in the multi-TeV energy range. The WCDA measurements fill the gap between direct detection by space telescopes and ultra-high-energy measurements by groundbased experiments, and offer a full energy coverage from GeV to PeV for the Galactic diffuse  $\gamma$ -ray emission. The SEDs of the diffuse emission in the two regions have been measured with high precision. The WCDA spectra are consistent with power-law models, with indices of  $-2.67 \pm 0.05_{\text{stat}}$  and  $-2.83 \pm 0.19_{\text{stat}}$ . The joint WCDA-KM2A spectrum shows a break around 30 TeV in the inner region, with indices changing by about 0.5. The break in the outer region is not signif-

<sup>1</sup> The prediction is based on a GALPROP model, which assumes a cylindrical propagation halo of the Milky Way, employs a numerical method to solve the transport equations, and includes experimental/observational inputs about the nuclear cross sections and gas distributions [2]. The prop-

agation and source injection parameters were adjusted to fit the up-to-date measurements of CR primary and secondary nuclei [35]. Note that, a homogeneous, isotropic diffusion is assumed when calculating the CR propagation, which may be over-simplified [36].

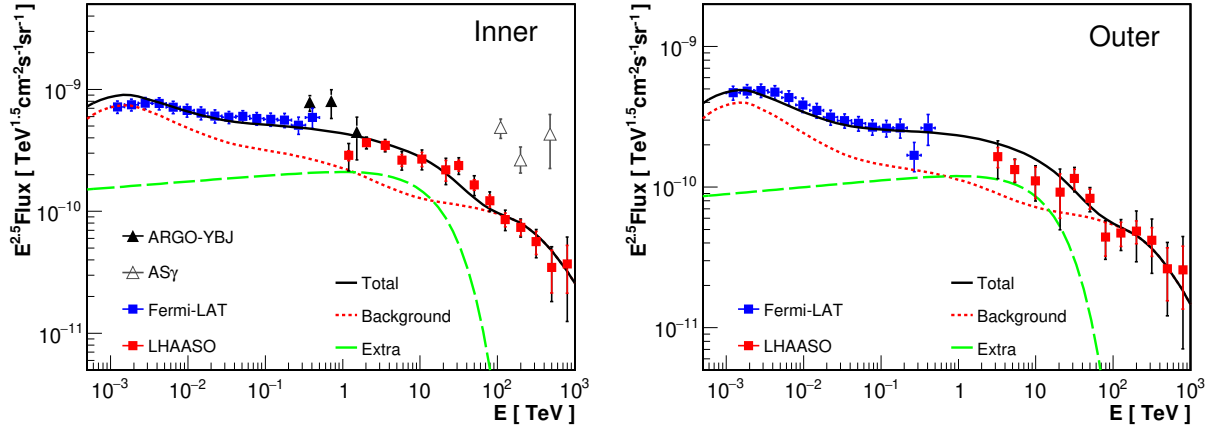


FIG. 5. Wide-band fluxes of diffuse  $\gamma$ -ray emission in the inner and outer Galaxy regions. To make the comparison more directly, the Fermi-LAT results with the same mask used in this work. The ARGO-YBJ and ASy data in the left panel are for a slightly different region of  $25^\circ < l < 100^\circ$  and  $|b| < 5^\circ$ , with different source masks [8, 9]. Red dotted lines show the prediction from a conventional CR propagation and interaction model [12], green dashed lines show the contribution from an assumed extra component, and black solid lines are the sum of these two components.

icant. We also show that there are slight spectral variations across the Galactic plane in the inner region. The measured fluxes are higher by a factor of 1.5 – 2.7 than the simple prediction of hadronic interactions between CRs and the ISM, indicating that there are unmodelled source components or spatial variations of CR distribution. The former is preferred if the low-energy measurements by Fermi-LAT and high-energy measurements by LHAASO-KM2A are taken into account.

*Acknowledgements.* — We would like to thank all staff members who work at the LHAASO site above 4400 meter above the sea level year-round to maintain the detector and keep the water recycling system, electricity power supply and other components of the experiment operating smoothly. We are grateful to Chengdu Management Committee of Tianfu New Area for the constant financial sup-

port for research with LHAASO data. We appreciate the computing and data service support provided by the National High Energy Physics Data Center for the data analysis in this paper. This work is supported by the following grants: the National Natural Science Foundation of China (Nos. 12220101003, 12173039, 12393851, 12393852, 12393853, 12393854, 12205314, 12105301, 12305120, 12261160362, 12105294, U1931201, 12375107), the Department of Science and Technology of Sichuan Province, China (No. 24NS-FSC2319), the Project for Young Scientists in Basic Research of Chinese Academy of Sciences (No. YSBR-061), the National Science and Technology Development Agency (NSTDA) of Thailand, and the National Research Council of Thailand (NRCT) under the High-Potential Research Team Grant Program (N42A650868).

- 
- [1] F. A. Aharonian and A. M. Atoyan, *Astron. Astrophys.* **362**, 937 (2000), astro-ph/0009009.
- [2] A. W. Strong, I. V. Moskalenko, and O. Reimer, *Astrophys. J.* **537**, 763 (2000), astro-ph/9811296.
- [3] A. W. Strong, I. V. Moskalenko, and O. Reimer, *Astrophys. J.* **613**, 962 (2004), astro-ph/0406254.
- [4] M. Ackermann, M. Ajello, W. B. Atwood, L. Baldini, J. Ballet, G. Barbiellini, D. Bastieri, K. Bechtol, R. Bellazzini, B. Berenji, et al., *Astrophys. J.* **750**, 3 (2012).
- [5] A. A. Abdo, B. Allen, D. Berley, E. Blaufuss, S. Casanova, C. Chen, D. G. Coyne, R. S. Delay, B. L. Dingus, R. W. Ellsworth, et al., *Astrophys. J. Lett.* **658**, L33 (2007), astro-ph/0611691.
- [6] A. A. Abdo, B. Allen, T. Aune, D. Berley, E. Blaufuss, S. Casanova, C. Chen, B. L. Dingus, R. W. Ellsworth, L. Fleysler, et al., *Astrophys. J.* **688**, 1078 (2008), 0805.0417.
- [7] A. Abramowski, F. Aharonian, F. Ait Benkhali, A. G. Akhperjanian, E. O. Angüner, M. Backes, S. Balenderan, A. Balzer, A. Barnacka, Y. Becherini, et al., *Phys. Rev. D* **90**, 122007 (2014), 1411.7568.
- [8] B. Bartoli, P. Bernardini, X. J. Bi, P. Branchini, A. Budano, P. Camarri, Z. Cao, R. Cardarelli, S. Catalanotti, S. Z. Chen, et al., *Astrophys. J.* **806**, 20 (2015), 1507.06758.
- [9] M. Amenomori, Y. W. Bao, X. J. Bi, D. Chen, T. L. Chen, W. Y. Chen, X. Chen, Y. Chen, Cirennima, S. W. Cui, et al., *Phys. Rev. Lett.* **126**, 141101 (2021).
- [10] R. Alfaro, C. Alvarez, J. C. Arteaga-Velázquez, K. P. Arunbabu, D. Avila Rojas, R. Babu, V. Baghmany, E. Belmont-Moreno, C. Brisbois, et al., *Astrophys. J.* **961**, 104 (2024), 2310.09117.
- [11] Z. Cao, F. Aharonian, Q. An, Y. X. Axikegu, Bai, Y. W. Bao, D. Bastieri, X. J. Bi, Y. J. Bi, J. T. Cai, Q. Cao, et al., *Phys. Rev. Lett.* **131**, 151001 (2023), 2305.05372.
- [12] R. Zhang, X.-Y. Huang, Z.-H. Xu, S.-P. Zhao, and Q. Yuan, *Astrophys. J.* **957**, 43 (2023), 2305.06948.

- [13] K. Yan, R.-Y. Liu, R. Zhang, C.-M. Li, Q. Yuan, and X.-Y. Wang, *Nature Astronomy* **8**, 628 (2024), 2307.12363.
- [14] Y.-H. Yao, X.-L. Dong, Y.-Q. Guo, and Q. Yuan, *Phys. Rev. D* **109**, 063001 (2024), 2308.15866.
- [15] K. Fang and K. Murase, *Astrophys. J. Lett.* **957**, L6 (2023), 2307.02905.
- [16] A. Dekker, I. Holst, D. Hooper, G. Leone, E. Simon, and H.-Y. Xiao, *Phys. Rev. D* **109**, 083026 (2024), 2306.00051.
- [17] X.-H. Ma, Y.-J. Bi, Z. Cao, M.-J. Chen, S.-Z. Chen, Y.-D. Cheng, G.-H. Gong, M.-H. Gu, H.-H. He, C. Hou, et al., *Chinese Physics C* **46**, 030001 (2022).
- [18] F. Aharonian, Q. An, Axikegu, L. X. Bai, Y. X. Bai, Y. W. Bao, D. Bastieri, X. J. Bi, Y. J. Bi, H. Cai, et al., *Chinese Physics C* **45**, 085002 (2021).
- [19] Z. Cao, F. Aharonian, Q. An, Axikegu, Y. X. Bai, Y. W. Bao, D. Bastieri, X. J. Bi, Y. J. Bi, J. T. Cai, et al., *Astrophys. J. Supp.* **271**, 25 (2024), 2305.17030.
- [20] A. U. Abeysekara, A. Albert, R. Alfaro, C. Alvarez, J. D. Álvarez, R. Arceo, J. C. Arteaga-Velázquez, H. A. Ayala Solares, and Barber, *Astrophys. J.* **843**, 39 (2017), 1701.01778.
- [21] R. Fleyscher, L. Fleyscher, P. Nemethy, A. I. Mincer, and T. J. Haines, *Astrophys. J.* **603**, 355 (2004), astro-ph/0306015.
- [22] H. E. S. S. Collaboration, H. Abdalla, A. Abramowski, F. Aharonian, F. Ait Benkhali, E. O. Angüner, M. Arakawa, M. Arrieta, P. Aubert, M. Backes, et al., *Astron. Astrophys.* **612**, A1 (2018), 1804.02432.
- [23] A. Albert, R. Alfaro, C. Alvarez, J. R. A. Camacho, J. C. Arteaga-Velázquez, K. P. Arunbabu, D. Avila Rojas, H. A. Ayala Solares, V. Baghmanyan, E. Belmont-Moreno, et al., *Astrophys. J.* **905**, 76 (2020), 2007.08582.
- [24] S. P. Wakely and D. Horan, *International Cosmic Ray Conference* **3**, 1341 (2008).
- [25] DAMPE Collaboration, G. Ambrosi, Q. An, R. Asfandiyarov, P. Azzarello, P. Bernardini, B. Bertucci, M. S. Cai, J. Chang, D. Y. Chen, et al., *Nature* **552**, 63 (2017), 1711.10981.
- [26] M. Aguilar, L. Ali Cavazonza, B. Alpat, G. Ambrosi, L. Arruda, N. Attig, P. Azzarello, A. Bachlechner, F. Barao, A. Barrau, et al., *Phys. Rev. Lett.* **122**, 101101 (2019).
- [27] O. Adriani, Y. Akaike, K. Asano, Y. Asaoka, E. Berti, G. Bigongiari, W. R. Binns, M. Bongi, P. Brogi, A. Bruno, et al., *Phys. Rev. Lett.* **131**, 191001 (2023), 2311.05916.
- [28] Icecube Collaboration, R. Abbasi, M. Ackermann, J. Adams, J. A. Aguilar, M. Ahlers, M. Ahrens, J. M. Alameddine, A. A. Alves, N. M. Amin, et al., *Science* **380**, 1338 (2023), 2307.04427.
- [29] HI4PI Collaboration, N. Ben Bekhti, L. Flöer, R. Keller, J. Kerp, D. Lenz, B. Winkel, J. Bailin, M. R. Calabretta, L. Dedes, et al., *Astron. Astrophys.* **594**, A116 (2016), 1610.06175.
- [30] T. M. Dame and P. Thaddeus, *Astrophys. J. Supp.* **262**, 5 (2022).
- [31] J. M. Cordes, J. M. Weisberg, D. A. Frail, S. R. Spangler, and M. Ryan, *Nature* **354**, 121 (1991).
- [32] M. Kachelrieß, I. V. Moskalenko, and S. Ostapchenko, *Computer Physics Communications* **245**, 106846 (2019), 1904.05129.
- [33] W. D. Apel, J. C. Arteaga-Velázquez, K. Bekk, M. Bertaina, J. Blümer, H. Bozdog, I. M. Brancus, E. Cantoni, A. Chiavassa, F. Cossavella, et al., *Astroparticle Physics* **47**, 54 (2013).
- [34] M. G. Aartsen, M. Ackermann, J. Adams, J. A. Aguilar, M. Ahlers, M. Ahrens, C. Alispach, K. Andeen, T. Anderson, I. Ansseau, et al., *Phys. Rev. D* **100**, 082002 (2019), 1906.04317.
- [35] Q. Yuan, C.-R. Zhu, X.-J. Bi, and D.-M. Wei, *J. Cosmol. Astropart. Phys.* **2020**, 027 (2020), 1810.03141.
- [36] G. Giacinti and D. Semikoz, arXiv e-prints arXiv:2305.10251 (2023), 2305.10251.
- [37] T. Linden and B. J. Buckman, *Phys. Rev. Lett.* **120**, 121101 (2018), 1707.01905.
- [38] G. Pagliaroli, S. Hussain, V. Vecchiotti, and F. L. Villante, *Universe* **9**, 381 (2023).
- [39] S. Menchiari, G. Morlino, E. Amato, N. Bucciantini, G. Peron, and G. Sacco, arXiv e-prints arXiv:2406.04087 (2024), 2406.04087.
- [40] R.-Z. Yang and F. Aharonian, *Phys. Rev. D* **100**, 063020 (2019), 1812.04364.
- [41] P.-P. Zhang, B.-Q. Qiao, Q. Yuan, S.-W. Cui, and Y.-Q. Guo, *Phys. Rev. D* **105**, 023002 (2022), 2107.08280.
- [42] X.-Y. He, P.-P. Zhang, Q. Yuan, and Y.-Q. Guo, *Astrophys. J.* **964**, 28 (2024), 2402.13467.
- [43] Y.-Q. Guo and Q. Yuan, *Phys. Rev. D* **97**, 063008 (2018), 1801.05904.
- [44] P. Lipari and S. Vernetto, *Phys. Rev. D* **98**, 043003 (2018), 1804.10116.
- [45] P. De La Torre Luque, D. Gaggero, D. Grasso, O. Fornieri, K. Egberts, C. Steppa, and C. Evoli, *Astron. Astrophys.* **672**, A58 (2023), 2203.15759.
- [46] S. Kaci and G. Giacinti, arXiv e-prints arXiv:2406.11015 (2024), 2406.11015.



## SUPPLEMENTAL MATERIAL

### A. Correction of large-scale structures

The background estimate method may introduce some large-scale structures due to the efficiency variation in a relatively long time window (10 hours). Similar phenomena have also been observed in the KM2A analysis [11]. We adopt the same method as that used in the KM2A analysis to correct these structures, via smoothing the ON and BKG counts map (after masking) with top-hat kernels, and then correct the background by multiplying smoothing  $N_{\text{on}}/N_{\text{BKG}}$  of each pixel. The benchmark radius of the smooth kernel is  $20^\circ$ , and other radii of  $15^\circ$ ,  $25^\circ$ ,  $30^\circ$  have been adopted to estimate the systematic uncertainty due to this correction. The significance maps before and after the correction of large-scale structures are shown in Fig. S1.

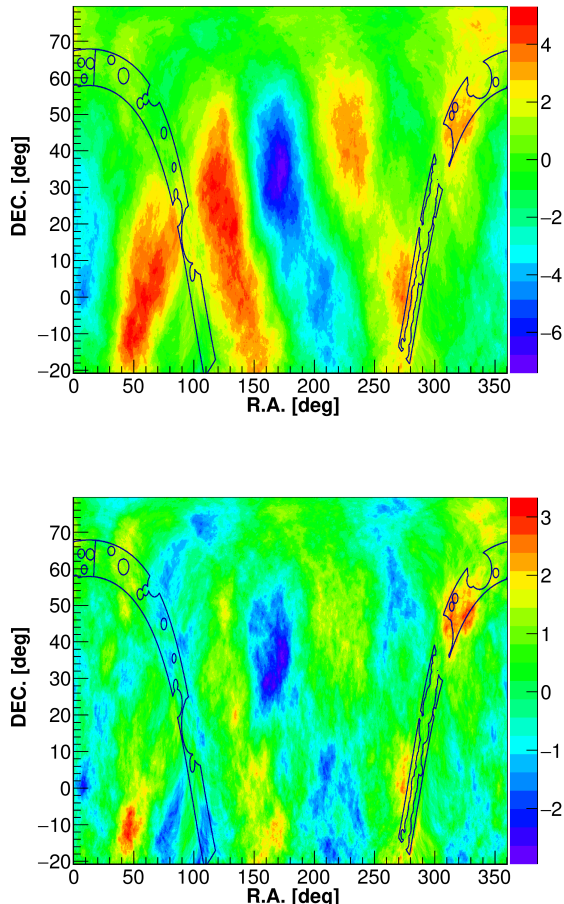


FIG. S1. Significance maps in celestial coordinate for  $N_{\text{hit}} \geq 100$ , before (top) and after (bottom) the large-scale structure correction. The black solid lines show the ROIs of this analysis.

### B. Residual contamination from resolved sources

There could be residual emission from known sources whose morphologies are assumed to be Gaussian, given the current mask radius of  $2.5\sigma$ . To estimate the contamination to diffuse emission from known sources, we divide the sky region into different rings around each source, with radius of each ring being a factor of  $n$  times of the source extension  $\sigma$ . The top panel of Fig. S2 illustrates the division of the sky. We construct two templates to fit the spatial distribution of events. One is the diffuse template from the gas distribution, and the other is the source template from all resolved sources weighted by their fluxes in corresponding energy band. The fitting result in one energy bin for the inner region is shown in the bottom panel of Fig. S2. The residual contamination can be obtained by setting  $n = 2.5$  as adopted in the analysis, which is given in Table S1. Such residual source contributions have been subtracted when deriving the diffuse emission fluxes.

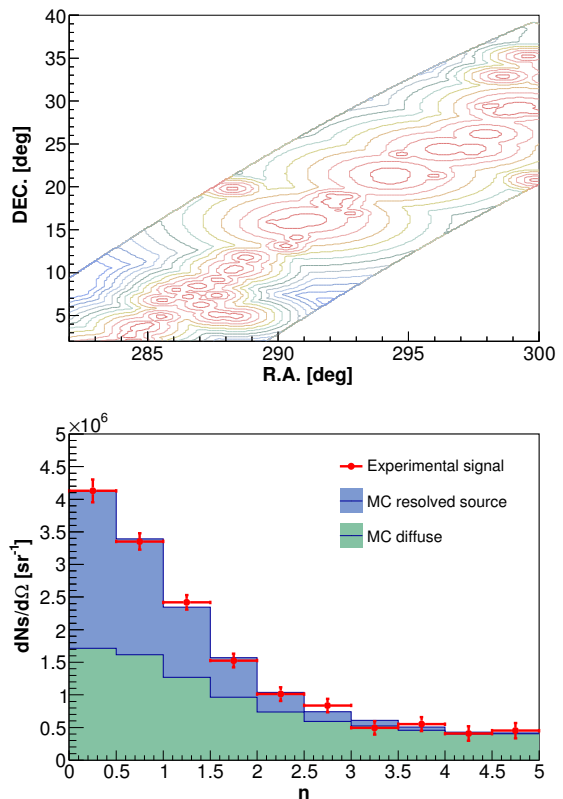


FIG. S2. Top: Schematic plot of sky regions of rings surrounding resolved sources. Bottom: Fitting results of the simulated signal intensities as functions of multiplicative factor  $n$  of the source extension  $\sigma$ , for resolved sources and diffuse emission.

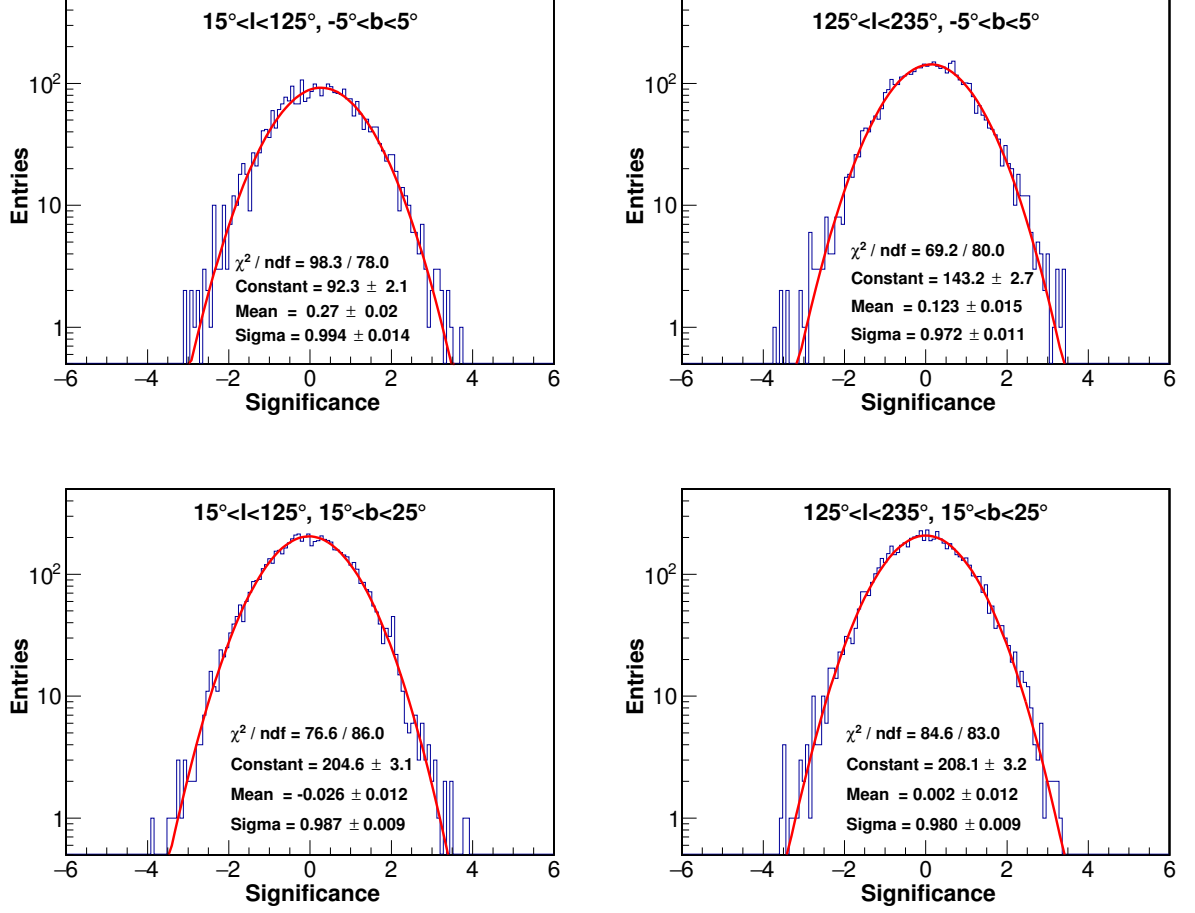


FIG. S3. One-dimensional significance distributions for  $N_{\text{hit}} \geq 200$  (corresponding to energies bigger than several TeV) after masking sources. Top two panels are for our ROIs, and bottom panels are the reference sky regions shifted to higher Galactic latitudes by 20 degrees.

TABLE S1. Residual fractions of resolved sources to the total signal in different hit bins.

$N_{\text{hit}}$	Inner Galaxy (%)	Outer Galaxy (%)
60-100	$11.12 \pm 0.19$	
100-200	$4.97 \pm 0.12$	
200-300	$3.76 \pm 0.18$	$1.57 \pm 0.10$
300-500	$3.36 \pm 0.21$	$1.10 \pm 0.09$
500-800	$3.07 \pm 0.31$	$1.18 \pm 0.20$
>800	$2.75 \pm 0.49$	$1.86 \pm 0.33$

### C. One-dimensional distributions of ROIs and control regions

The one-dimensional significance distributions of our analyzed ROIs are presented in top panels of Fig. S3. The positive mean values of the significance in both regions indicate the detection of diffuse emission. As a comparison, the one-dimensional significance distributions in control regions, shifted along the Galactic latitudes by  $20^\circ$ , are shown in bottom panels. The results in control regions are consistent with

the standard Gaussian distribution as expected for the background.

### D. Fluxes of diffuse emission measured by LHAASO

The diffuse emission fluxes of the inner and outer Galaxy regions measured by LHAASO, together with  $1\sigma$  statistical errors and the estimated systematic uncertainties, are presented in Tables S2 and S3.

We compare the measured diffuse  $\gamma$ -ray fluxes with the total fluxes of CR electrons plus positrons in Fig. S4. Although the electron and positrons fluxes are higher than the diffuse  $\gamma$ -ray emission by a factor of several below several TeV, they are largely removed with our data-driven background estimate method as long as electrons and positrons do not concentrate in the Galactic plane as  $\gamma$  rays.

Fig. S5 shows the fluxes of all emission in the ROIs without source masks.

TABLE S2. Diffuse emission fluxes in the inner Galaxy region measured by WCDA-KM2A, together with  $1\sigma$  statistical uncertainties and systematic uncertainties.

$\langle E \rangle$ (TeV)	$\phi \pm \sigma_{\text{stat}} \pm \sigma_{\text{sys}}$ ( $\text{TeV}^{-1} \text{cm}^{-2} \text{s}^{-1} \text{sr}^{-1}$ )
1.20	$(2.07 \pm 0.27 \pm 0.49) \times 10^{-10}$
2.03	$(6.84 \pm 0.47 \pm 0.60) \times 10^{-11}$
3.54	$(1.57 \pm 0.14 \pm 0.11) \times 10^{-11}$
5.81	$(3.35 \pm 0.37 \pm 0.45) \times 10^{-12}$
10.55	$(7.52 \pm 0.99 \pm 0.99) \times 10^{-13}$
21.53	$(1.01 \pm 0.20 \pm 0.15) \times 10^{-13}$
31.62	$(4.21 \pm 0.44 \pm 0.49) \times 10^{-14}$
50.12	$(9.90 \pm 0.97 \pm 1.57) \times 10^{-15}$
79.43	$(2.35 \pm 0.27 \pm 0.34) \times 10^{-15}$
125.89	$(5.19 \pm 0.67 \pm 0.73) \times 10^{-16}$
199.53	$(1.41 \pm 0.21 \pm 0.12) \times 10^{-16}$
316.23	$(3.36 \pm 0.72 \pm 0.50) \times 10^{-17}$
501.19	$(6.48 \pm 2.48 \pm 1.84) \times 10^{-18}$
794.33	$(2.17 \pm 0.92 \pm 1.10) \times 10^{-18}$

TABLE S3. Diffuse emission fluxes in the outer Galaxy region measured by WCDA-KM2A, together with  $1\sigma$  statistical uncertainties and systematic uncertainties.

$\langle E \rangle$ (TeV)	$\phi \pm \sigma_{\text{stat}} \pm \sigma_{\text{sys}}$ ( $\text{TeV}^{-1} \text{cm}^{-2} \text{s}^{-1} \text{sr}^{-1}$ )
3.23	$(8.72 \pm 1.43 \pm 2.20) \times 10^{-12}$
5.36	$(2.00 \pm 0.36 \pm 0.13) \times 10^{-12}$
9.91	$(3.58 \pm 0.90 \pm 0.44) \times 10^{-13}$
20.59	$(4.76 \pm 1.65 \pm 1.44) \times 10^{-14}$
31.62	$(2.03 \pm 0.33 \pm 0.22) \times 10^{-14}$
50.12	$(4.66 \pm 0.76 \pm 0.51) \times 10^{-15}$
79.43	$(7.81 \pm 2.09 \pm 1.18) \times 10^{-16}$
125.89	$(2.64 \pm 0.52 \pm 0.40) \times 10^{-16}$
199.53	$(8.60 \pm 1.59 \pm 2.99) \times 10^{-17}$
316.23	$(2.35 \pm 0.54 \pm 0.82) \times 10^{-17}$
501.19	$(4.67 \pm 1.91 \pm 1.64) \times 10^{-18}$
794.33	$(1.45 \pm 0.69 \pm 0.80) \times 10^{-18}$

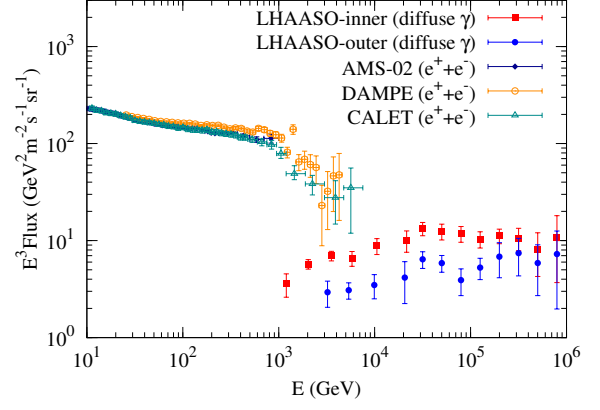


FIG. S4. Comparison of the diffuse  $\gamma$ -ray fluxes measured by LHAASO with the total electron plus positron fluxes by several experiments [25-27].

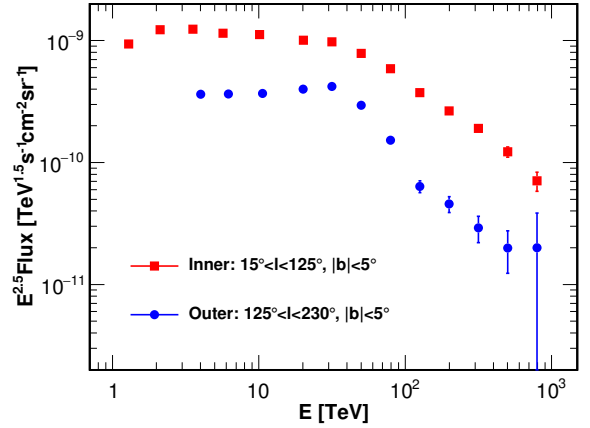


FIG. S5. SEDs of all the  $\gamma$ -ray emission in the inner and outer regions without source masks. Error bars are the statistical errors.

### E. Comparison of longitude and latitude distributions with KM2A

Fig. S6 shows the comparison of longitude and latitude distributions of the WCDA measurements with the KM2A results. The trends of the data in the two different energy bands are similar with each other. Difference of the longitude distributions in some longitude bins (e.g.,  $65^\circ < l < 85^\circ$ ) are likely due to different source masks in the two analyses.

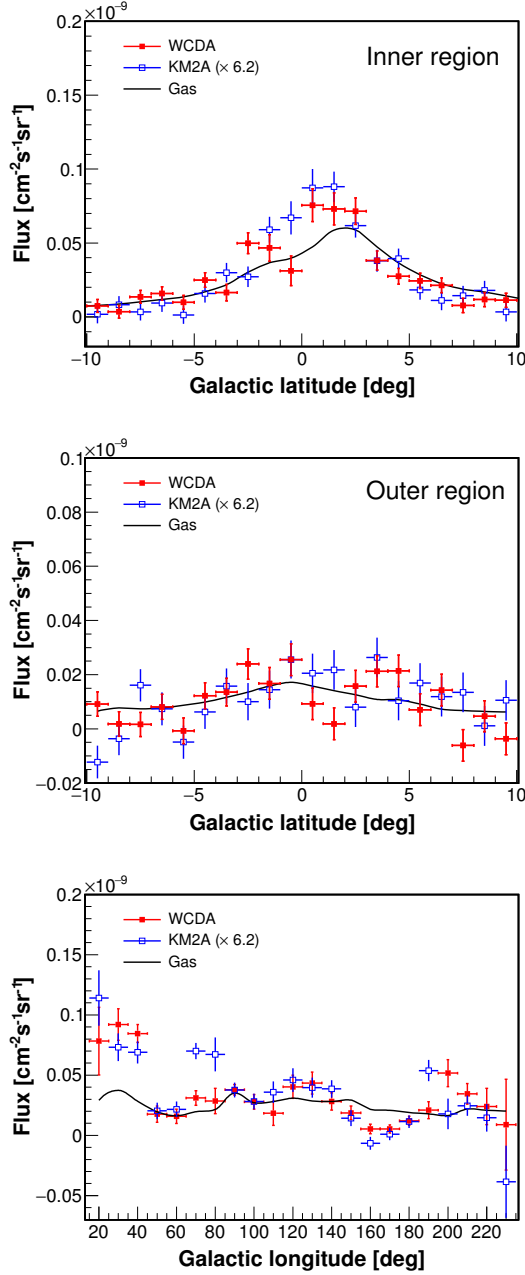


FIG. S6. Comparison of the latitude and longitude profiles of the WCDA (red points) and KM2A (blue points) measurements. The KM2A data for the 10 – 63 TeV band are plotted [11].